

Stabilized adaptive waveform inversion for enhanced robustness in Gaussian penalty matrix parameterization and transcranial ultrasound imaging

Jun-Jie Zhao(赵俊杰), Shan-Mu Jin(金山木), Yue-Kun Wang(王月坤), Yu Wang(王裕), and Ya-Hui Peng(彭亚辉)
Citation: Chin. Phys. B, 2025, 34 (**8**): 084301. DOI: 10.1088/1674-1056/add4f3
http://cpb.iphy.ac.cn; http://iopscience.iop.org/cpb

What follows is a list of articles you may be interested in

Sobolev space norm regularized full waveform inversion for ultrasound computed tomography

Panpan Li(李盼盼), Yubing Li(李玉冰), Chang Su(苏畅), Zeyuan Dong(董则元), and Weijun Lin(林伟军)
Chin. Phys. B, 2025, 34 (**5**): 054301. DOI: 10.1088/1674-1056/adbbc0

Multi-parameter ultrasound imaging for musculoskeletal tissues based on a physics informed generative adversarial network

Pengxin Wang(王鹏鑫), Heyu Ma(马贺雨), Tianyu Liu(刘天宇), Chengcheng Liu(刘成成), Dan Li(李旦), and Dean Ta(他得安)
Chin. Phys. B, 2025, 34 (**4**): 044301. DOI: 10.1088/1674-1056/adb390

Discrete multi-step phase hologram for high frequency acoustic modulation

Meng-Qing Zhou(周梦晴), Zhao-Xi Li(李照希), Yi Li(李怡), Ye-Cheng Wang(王业成), Juan Zhang(张娟), Dong-Dong Chen(谌东东), Yi Quan(全熠), Yin-Tang Yang(杨银堂), and Chun-Long Fei(费春龙)
Chin. Phys. B, 2024, 33 (**1**): 014303. DOI: 10.1088/1674-1056/acf44c

Tunable topological interface states and resonance states of surface waves based on the shape memory alloy

Shao-Yong Huo(霍绍勇), Long-Chao Yao(姚龙超), Kuan-Hong Hsieh(谢冠宏), Chun-Ming Fu(符纯明), Shih-Chia Chiu(邱士嘉), Xiao-Chao Gong(龚小超), and Jian Deng(邓健)
Chin. Phys. B, 2023, 32 (**3**): 034303. DOI: 10.1088/1674-1056/ac8727

Quantitative ultrasound brain imaging with multiscale deconvolutional waveform inversion

Yu-Bing Li(李玉冰), Jian Wang(王建), Chang Su(苏畅), Wei-Jun Lin(林伟军), Xiu-Ming Wang(王秀明), and Yi Luo(骆毅)
Chin. Phys. B, 2023, 32 (**1**): 014303. DOI: 10.1088/1674-1056/ac6dad

---

Stabilized adaptive waveform inversion for enhanced robustness in Gaussian penalty matrix parameterization and transcranial ultrasound imaging

Jun-Jie Zhao(赵俊杰)[1,†], Shan-Mu Jin(金山木)[2,†], Yue-Kun Wang(王月坤)[2], Yu Wang(王裕)[2,‡], and Ya-Hui Peng(彭亚辉)[1,§]

[1] *School of Electronic and Information Engineering, Beijing Jiaotong University, Beijing* 100044, *China*

[2] *Department of Neurosurgery, Center for Malignant Brain Tumors, National Glioma MDT Alliance, Peking Union Medical College Hospital, Chinese Academy of Medical Sciences and Peking Union Medical College, Beijing* 100730, *China*

(Received 23 January 2025; revised manuscript received 29 April 2025; accepted manuscript online 7 May 2025)

Achieving high-resolution intracranial imaging in a safe and portable manner is critical for the diagnosis of intracranial diseases, preoperative planning of craniotomies and intraoperative management during craniotomy procedures. Adaptive waveform inversion (AWI), a variant of full waveform inversion (FWI), has shown potential in intracranial ultrasound imaging. However, the robustness of AWI is affected by the parameterization of the Gaussian penalty matrix and the challenges posed by transcranial scenarios. Conventional AWI struggles to produce accurate images in these cases, limiting its application in critical medical settings. To address these issues, we propose a stabilized adaptive waveform inversion (SAWI) method, which introduces a user-defined zero-lag position for the Wiener filter. Numerical experiments demonstrate that SAWI can achieve accurate imaging under Gaussian penalty matrix parameter settings where AWI fails, perform successful transcranial imaging in configurations where AWI cannot, and maintain the same imaging accuracy as AWI. The advantage of this method is that it achieves these advancements without modifying the AWI framework or increasing computational costs, which helps to promote the application of AWI in medical fields, particularly in transcranial scenarios.

Keywords: ultrasound brain imaging, full waveform inversion, robustness, parameterization

PACS: 43.60.Lq, 43.80.Qf, 43.35.Wa, 87.63.dh

DOI: 10.1088/1674-1056/add4f3 **CSTR:** 32038.14.CPB.add4f3

1. Introduction

Intracranial imaging plays a critical role in medicine since it enables the diagnosis and evaluation of brain disorders. It is commonly employed in scenarios such as diagnosis of intracranial hemorrhages, strokes, preoperative localization of intracranial tumors, and intraoperative tumor resection.

Currently, intracranial imaging techniques can be categorized into two types. The first category includes methods that utilize natural openings in the skull[1,2] or create a bony window by surgically opening a portion of the skull to perform internal imaging with an ultrasound probe. The first category is summarized as invasive imaging. The second category comprises non-invasive imaging techniques that involve external imaging equipment, such as computed tomography (CT) or magnetic resonance imaging (MRI), to observe and diagnose intracranial conditions without the need for puncture or surgical procedures. The second category is summarized as non-invasive imaging. Both existing methods have limitations.

Invasive imaging Traditional medical ultrasound is a rapid, safe and affordable imaging technique, which seems well-suited for transcranial imaging.[3] However, this method is encumbered by a series of technical shortcomings. The former (natural opening) imposes significant constraints on illumination, given that the natural acoustic window in the skull is present only in a limited number of locations; the quality of the ultrasound image is problematic, resulting in interpretation that is usually dependent on the physician using the imaging equipment, who may encounter difficulties in identifying tissue edema and tumors; small lesions may also be difficult to detect; furthermore, blood and hemostatic medications in the resection cavity can confound image interpretation.[1] In addition to technical issues, the invasive approach can have an impact on postoperative recovery time.

Non-invasive imaging Non-invasive intracranial imaging, including CT and MRI, facilitates high-resolution imaging of the intracranial region and is extensively utilized.[4–6] However, both modalities have significant limitations in their application. Both methods necessitate the use of large, costly, immobile, high-powered instruments, which are impractical to deploy outside of a specialized setting.[3,7] This results in a considerable delay between symptom onset and imaging, which can have a substantial impact on outcomes in diseases

[†]These authors contributed equally to this work.

[‡]Corresponding author. E-mail: ywang@pumch.cn

[§]Corresponding author. E-mail: yhpeng@bjtu.edu.cn

© 2025 Chinese Physical Society and IOP Publishing Ltd. All rights, including for text and data mining, AI training, and similar technologies, are reserved.

such as stroke.[8] For CT, the use of ionizing radiation poses a significant concern, particularly for pregnant women and children.[9] The low soft tissue contrast can limit the ability to discern details, particularly in cases of small or low contrast abnormalities. For MRI, which is regarded as the modality offering the best spatial resolution and tissue contrast, its use is contraindicated in situations where the presence of magnetic foreign bodies cannot be ruled out. MRI is also impractical for patients who are claustrophobic, uncooperative or severely obese.[7] In addition, brain tissue drift represents a significant limitation when MRI and CT are employed. The soft nature of brain tissue can result in its displacement when the patient's positioning during preoperative MRI/CT differs from that during surgery, as evidenced by intraoperative ultrasound and MRI.[10–13] This deviation may result in a mismatch between the preoperative planning based on imaging and the real-time intraoperative anatomy, thus compromising surgical precision and increasing operational difficulty.

To bridge the gap between the real-time, safe and low-cost advantages of ultrasound and the high-resolution capabilities of MRI and CT, full waveform inversion (FWI), a technique originally developed in geophysics, is gaining increasing attention in the medical imaging field. FWI is a seismic data inversion technique designed to recover high-resolution models of subsurface physical properties by minimizing mismatches between predicted data simulated using acoustic velocity models and observed data.[14] Early developments in the 1970s and 1980s focused on iteratively fitting full time series based on physical model parameters. With the advancement of computational capabilities, FWI has become a major focus in seismic exploration, playing a crucial role in retrieving detailed subsurface structures.[15] In recent years, FWI has been gradually introduced into the medical field. This technique has already demonstrated its potential for imaging the breast, limbs and human brain.[3,16–18] The spatial resolution of FWI imagery is approximately half a wavelength, corresponding to millimeters or sub-millimeters at sub-megahertz frequencies. The primary factor enabling such high-precision imaging is that FWI simulates acoustic wave propagation by numerically solving the wave equation, taking into account not only the weak scattering from soft tissues but also the strong reflection, refraction and multiple scattering induced by bone.[19] FWI combines this accurate physical modeling with a suitable nonlinear inversion scheme and appropriate data acquisition geometry, enabling the recovery of fine heterogeneity throughout the model.

However, conventional FWI is a local optimization algorithm that requires an initial model located within the attractive range of the global minimum. When the time lag between observed and predicted data exceeds half a cycle, conventional FWI falls into a local minimum, a phenomenon known as cycle skipping, as detailed in a previous study.[20] For imaging targets, such as the breast, where sound velocity values range from 1400 m/s to 1600 m/s, FWI performs well when using a homogeneous water model with a sound speed of 1500 m/s as the initial background. However, for the cranium, the acoustic velocity of cortical bone can reach 2800 m/s. The resulting mismatch with a water-based model, along with strong reflections at the soft tissue–skull interface, presents substantial challenges for imaging.[21,22]

Current approaches to addressing this issue primarily fall into four categories: utilizing a more accurate initial model, inverting with low-frequency data, employing global or semi-global FWI, and developing novel objective functions that are less sensitive to cycle skipping. While the first approach is practical, reducing FWI's dependence on an accurate initial model remains a longstanding challenge and is therefore not discussed further. The second approach relies on the long wavelengths of low-frequency waves. This makes it less likely for multiple oscillatory cycles to appear within the limited time window of ultrasound data, reducing the chance of cycle skipping. In addition, low-frequency waves penetrate the skull more effectively, improving the imaging of intracranial structures. However, most current medical ultrasound probes are not designed for imaging at frequencies below 1.00 MHz, resulting in a lack of low-frequency components in the received signals.[23] For the third approach, the most direct way to mitigate the risk of local minimum is to employ global or semi-global FWI strategies. Unlike conventional local FWI, these methods do not require computing the derivative of the objective function, making them applicable to a wide range of objective functions, even those that are non-differentiable or discontinuous.[24] Under certain constraints, these approaches explore the model space by introducing random perturbations to the parameters and guiding convergence through stochastic processes to seek a globally optimal solution. However, due to the high dimensionality of the FWI model space, the computational cost of global optimization remains prohibitively expensive, even for 2D inversions.

The study of Guasch *et al.* revealed that FWI struggled to achieve successful inversion from a water-initialized model when applied to 3D ultrasound data, whereas adaptive waveform inversion (AWI) demonstrated superior performance.[3] This finding prompts further investigation. AWI, a variant of FWI, is designed to address the cycle skipping phenomenon by minimizing the time lag between observed and predicted data rather than the residuals between them. While AWI can successfully image with an initial model significantly different from the target model, it has certain limitations. AWI is more nonlinear than FWI and prone to Wiener filter polarity reversal during iterations, causing it to deviate from the imaging target and fall into local minimum. Pladys *et al.*[25] indicated that

the choice of parameters in the Gaussian penalty matrix has a significant impact on whether AWI can successfully image, which has drawn our attention. In their experiment designed for reflected waves, it was observed that AWI failed to produce satisfactory imaging results when the parameter σ of the Gaussian penalty matrix was set to 1 s. However, when σ was reduced to below 0.04 s, the imaging results became comparable to those of the normalized integration method.

This issue is highly research-worthy, as the Gaussian penalty matrix is a common choice in conventional AWI practice due to its advantage in convergence speed compared to linear penalty matrix.[14] Moreover, the choice of σ does not simply affect the convergence speed but also determines whether imaging can succeed. In simulation experiments with known imaging targets, parameters can be adjusted according to the ground truth to achieve successful imaging. However, in cases of unknown imaging targets, particularly in fault-intolerant medical imaging scenarios, it is impossible to adjust parameters to obtain what might be deemed a reasonable imaging result. In our practice, we encountered such situations and found that under incorrect parameters, the Wiener filter in AWI exhibited polarity reversal, meaning that imaging could not return to the correct trajectory despite increased iterations. In addition, due to the high acoustic impedance at the soft tissue–skull interface in transcranial scenarios,[26] the ultrasonic signals received by transducers in these cases are dominated by reflected waves. We observed that AWI faced significant challenges in transcranial imaging, regardless of whether linear or Gaussian penalty matrices were used.

In this paper, to address the two aforementioned issues, we propose a stabilized adaptive waveform inversion (SAWI) method by introducing a user-defined zero-lag position for the Wiener filter. This approach mitigates the impact of Gaussian penalty matrix parameterization on the robustness of the AWI algorithm. Simulation results demonstrate that SAWI resolves the imaging challenges of AWI in transcranial scenarios while retaining the same imaging accuracy as AWI. Importantly, this method does not require modifications to the AWI framework and incurs no additional computational burden in practice.

The remainder of this paper is organized as follows. In Section 2, we first introduce the theoretical foundations of conventional FWI, conventional AWI and the proposed SAWI method, followed by a description of the numerical experiments included in this paper. In Section 3, we present the results of the numerical experiments to demonstrate the effectiveness of the proposed method. Finally, in Section 4, we provide a discussion of the experimental results, examine the possible reasons for the effectiveness of the proposed method, and outline several limitations of this paper.

2. Methods

In this section, we introduce the classical full waveform inversion and adaptive inversion algorithms and present a novel AWI method. Details of the numerical experiments are also described.

2.1. FWI algorithm

FWI is an imaging method that aims to find models that can reproduce experimental data numerically. It accomplishes this by solving a nonlinear least-squares optimization problem, where the numerical sound velocity model is modified during the optimization iterations to minimize the mismatch function f. f is defined as the second-paradigm number of the residuals between the predicted data p, generated numerically using a numerical model m of the acoustic properties, and the observed data d. The objective of FWI is to minimize f, the difference between the observed and predicted data, in order to make the numerical sound velocity model close to the real imaging target region. FWI is essentially a local optimization problem with three main components: the physical process simulating acoustic wave propagation, the objective function and gradient, and the iteration of the model.

2.1.1. Physical process

The isotropic wave equation is employed in this paper and is expressed as

$$\frac{1}{m(x)^2}\frac{\partial^2 u(x,t)}{\partial t^2} - \rho(x)\nabla\cdot\left(\frac{1}{\rho(x)}\nabla u(x,t)\right) = s(x_s,t), \quad (1)$$

where $m(x)$ denotes the compressional velocity field, $u(x,t)$ represents the pressure field (i.e., the wavefield), $s(x_s,t)$ corresponds to the source term applied at the source location x_s, and $\rho(x)$ refers to the density. Independent variables x and t correspond to location and time variables, respectively.

2.1.2. Objective function and gradient

To facilitate understanding, all algorithmic derivations in this section are explained in matrix form. The objective function f of FWI is the L2-norm of the residual between the predicted data $\boldsymbol{p}$ and the observed data $\boldsymbol{d}$, with the goal of minimizing this residual.

$$f = \frac{1}{2}(\boldsymbol{p}-\boldsymbol{d})^{\mathrm{T}}(\boldsymbol{p}-\boldsymbol{d}), \quad (2)$$

where the simulated data $\boldsymbol{p}$ represents the wavefield at the positions of the receivers. The relationship between $\boldsymbol{u}$ and $\boldsymbol{p}$ in matrix form is written as

$$\boldsymbol{R}\boldsymbol{u} = \boldsymbol{p}, \quad (3)$$

where $\boldsymbol{R}$ is the positioning operator. The derivative of f with respect to $\boldsymbol{m}$ is as follows, consisting of two parts. The derivative of f with respect to $\boldsymbol{p}$ is the residual between $\boldsymbol{p}$ and $\boldsymbol{d}$.

Therefore, the key to calculating the gradient lies in the partial derivative of $\boldsymbol{p}$ with respect to $\boldsymbol{m}$

$$\frac{\partial f}{\partial \boldsymbol{m}_i} = \left[\frac{\partial \boldsymbol{p}}{\partial \boldsymbol{m}_i}\right]^{\mathrm{T}} \frac{\partial f}{\partial \boldsymbol{p}}, \tag{4}$$

$$\frac{\partial f}{\partial \boldsymbol{p}} = \boldsymbol{p} - \boldsymbol{d}. \tag{5}$$

To better understand the process of gradient computation, the wave equation is discretized into the following form:

$$\boldsymbol{A}\boldsymbol{u} = \boldsymbol{s}, \tag{6}$$

where $\boldsymbol{A}$ is the wave equation operator. Since $\boldsymbol{s}$ does not depend on $\boldsymbol{m}$, it can be expressed as

$$\boldsymbol{A}\frac{\partial \boldsymbol{u}}{\partial \boldsymbol{m}_i} + \frac{\partial \boldsymbol{A}}{\partial \boldsymbol{m}_i}\boldsymbol{u} = 0. \tag{7}$$

By transforming the equation and incorporating the relationship between $\boldsymbol{p}$ and $\boldsymbol{u}$, the partial derivative of $\boldsymbol{p}$ with respect to $\boldsymbol{m}$ is obtained as follows:

$$\frac{\partial \boldsymbol{p}}{\partial \boldsymbol{m}_i} = -\boldsymbol{R}\boldsymbol{A}^{-1}\frac{\partial \boldsymbol{A}}{\partial \boldsymbol{m}_i}\boldsymbol{u}. \tag{8}$$

Thus, the partial derivative of f with respect to $\boldsymbol{m}$ is as follows, which constitutes the gradient:

$$\frac{\partial f}{\partial \boldsymbol{m}_i} = -\boldsymbol{u}^{\mathrm{T}}\frac{\partial \boldsymbol{A}^{\mathrm{T}}}{\partial \boldsymbol{m}_i}\boldsymbol{A}^{-\mathrm{T}}\boldsymbol{R}^{\mathrm{T}}(\boldsymbol{p}-\boldsymbol{d}). \tag{9}$$

2.1.3. Model iteration

Since the relationship between the data and the model is nonlinear, multiple iterations of the above process are required to converge to the minimum of the mismatch function. The model iteration can be expressed as

$$m_{i+1} = m_i + \alpha_i d_i, \tag{10}$$

where m represents the velocity model, α is the step size and d is the update direction. In this paper, we employ the gradient descent method, where α is a linear step size and d is the original gradient preconditioned by the diagonal elements of the approximate Hessian matrix.[24] The iteration terminates when the predefined number of iterations is reached.

2.2. AWI algorithm

To facilitate understanding, all algorithmic derivations in this section are explained in matrix form. The paper focuses on and investigates forward AWI.[27] All explanations of the AWI algorithm are based on single-trace data. The framework of AWI is identical to that of FWI, with the key difference lying in the objective function. Unlike FWI, which aims to minimize the residual between predicted and observed data, AWI minimizes the time shift between the two data. AWI constructs a Wiener filter that makes the predicted data approximate the observed data to reflect this time-shift and amplitude relationship. The solution for $\boldsymbol{w}$ in matrix form is shown as

$$\boldsymbol{w} = (\boldsymbol{P}^{\mathrm{T}}\boldsymbol{P} + \lambda \boldsymbol{I})^{-1}\boldsymbol{P}^{\mathrm{T}}\boldsymbol{d}, \tag{11}$$

where $\boldsymbol{P}$ is the Toeplitz matrix with each column representing the predicted data $\boldsymbol{p}$, controlling the length of $\boldsymbol{w}$; λ is the regularization coefficient, typically set between 10^{-2} and 10^{-5}, to stabilize the solution of $\boldsymbol{w}$; and $\boldsymbol{d}$ represents the observed data, which needs to be zero-padded to conform to the rules of matrix computation. The peak position of the Wiener filter reflects the time shift between the predicted and observed data. Based on the different zero-padding methods for $\boldsymbol{d}$, there is a user-definable zero-lag position on $\boldsymbol{w}$. In conventional AWI, this position is defined at the center of $\boldsymbol{w}$. The difference between the peak position of $\boldsymbol{w}$ and the zero-lag position reflects the lag relationship between the predicted data and the observed data. Therefore, the objective of AWI is to shift the peak of the Wiener filter to the zero-lag position. The corresponding objective function in matrix form is written as

$$f = \frac{1}{2}\frac{\|\boldsymbol{T}\boldsymbol{w}\|^2}{\|\boldsymbol{w}\|^2}, \tag{12}$$

where $\boldsymbol{T}$ is the penalty matrix. A Gaussian penalty matrix is used in this paper, which is written as

$$\boldsymbol{T} = \mathrm{e}^{-\frac{\tau^2}{\sigma^2}}, \tag{13}$$

where τ is the time lag and σ is a tuning parameter that controls the spread of the Gaussian function along the time-lag axis. When the penalty value is maximized at the zero-lag position and decreases as the lag increases, the AWI objective function should be maximized; otherwise, the opposite approach is applied. In this paper, we adopt the maximization approach.

Since the objective function is modified, the gradient of the objective function with respect to the velocity model $\boldsymbol{m}$ also changes. As the partial derivative of $\boldsymbol{p}$ with respect to $\boldsymbol{m}$ originates from the wave equation, only the derivative of the objective function with respect to $\boldsymbol{p}$ (i.e., the adjoint source) is affected. The solution for the adjoint source in matrix form is as follows:

$$\frac{\partial f}{\partial \boldsymbol{p}} = \boldsymbol{W}^{\mathrm{T}}\boldsymbol{P}\left(\boldsymbol{P}^{\mathrm{T}}\boldsymbol{P}\right)^{-1}\left(\frac{2f\boldsymbol{I} - \boldsymbol{T}^2}{\boldsymbol{w}^{\mathrm{T}}\boldsymbol{w}}\right)\boldsymbol{w}, \tag{14}$$

where $\boldsymbol{W}$ is the Toeplitz matrix with each column representing $\boldsymbol{w}$.

In summary, the practical differences between AWI and FWI lie in two aspects: replacing the objective function and modifying the adjoint source. The computation of $\boldsymbol{w}$ can be performed implicitly.

2.3. SAWI algorithm

As noted in the introduction to AWI, the observed data $\boldsymbol{d}$ needs to be zero-padded to conform to matrix computation rules. We observed that different zero-padding methods influence the location of the zero-lag position in the constructed Wiener filter $\boldsymbol{w}$. In the conventional AWI, the zero-lag position is typically located at the center of $\boldsymbol{w}$.

We found that placing the constructed zero-lag position at the edge of $\boldsymbol{w}$ can provide robustness not observed in conventional AWI under identical experimental conditions, though at the expense of accuracy. This finding can be used to construct a suitable initial model for scenarios in which conventional AWI fails to converge or produce meaningful images. Based on this observation, we developed SAWI, a two-step approach. In the first step, a Wiener-based inversion with the zero-lag position set at the edge of $\boldsymbol{w}$ is used to generate an initial model. This model is then used to initialize conventional AWI, where the zero-lag position is centered, for refined imaging (Fig. 1).

We define the 'node' as the transition point between two imaging stages in SAWI. Before the node, the Wiener filter is constructed with the zero-lag position at the left edge to perform initial imaging. After the node, conventional AWI is applied, with the zero-lag position centered, for high-resolution refinement. The number of iterations before and after the node can be customized according to imaging requirements. Since SAWI employs conventional AWI for imaging after the node, the imaging accuracy of SAWI is equivalent to that of AWI. The primary objective of SAWI is to improve the robustness of AWI when dealing with Gaussian penalty matrix parameterization and transcranial imaging scenarios.

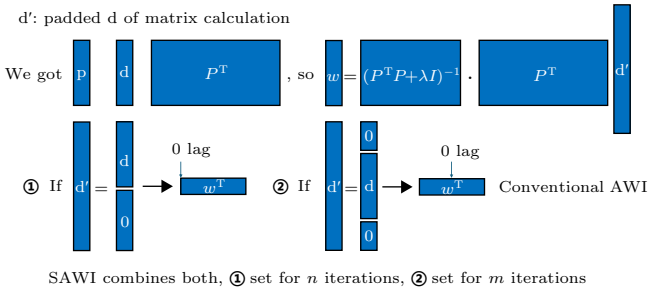


Fig. 1. SAWI schematic diagram.

2.4. Velocity models

All experiments in this paper are 2D numerical simulations. To evaluate SAWI's performance under different Gaussian penalty parameter settings, its effectiveness in transcranial imaging, and its imaging accuracy, we designed three target velocity models: a block model, a cranial model and a cranium–block hybrid model. Details of the target velocity models are introduced below.

Block model As shown in Fig. 2(a), the model size is 356×385 with a grid spacing of 500 μm. It contains two targets: a square located at (110,110) with a side length of

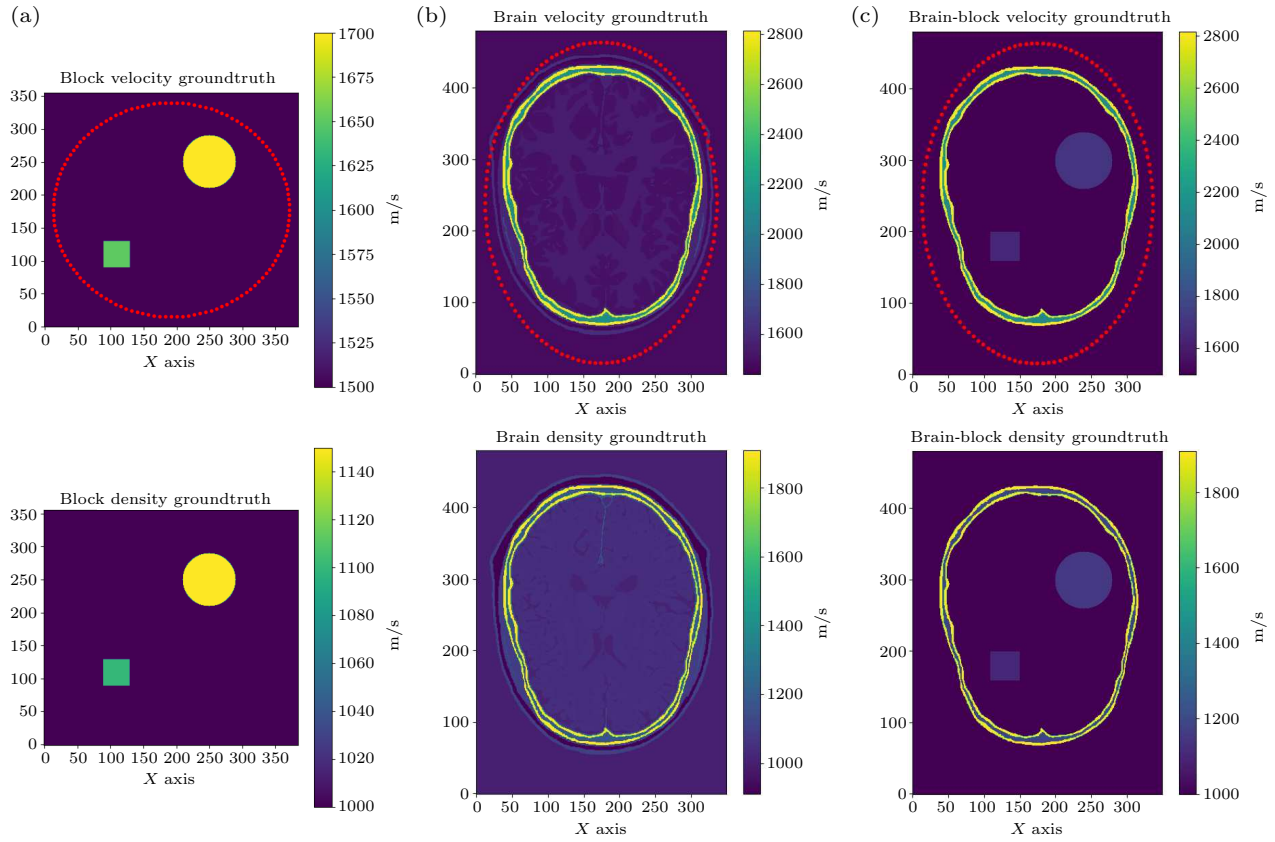


Fig. 2. Velocity (with transducer array) and density models of (a) block model, (b) cranial model and (c) cranium–block model used in the paper.

40 grid points, and a circle centered at (250, 250) with a radius of 40. The square has a velocity of 1650 m/s and a density of 1100 kg/m^3, while the circular target has a velocity of 1700 m/s and a density of 1150 kg/m^3. The background medium has a velocity of 1500 m/s and a density of 1000 kg/m^3. The simulation was performed with 4.108 points per wavelength (PPW) and a Courant–Friedrichs–Lewy (CFL) number of 0.27.[28]

Cranial model The MIDA model was used as the original numerical model of the cranium.[29] It has a size of $480 \times 480 \times 350$ with a grid spacing of 500 μm. After assigning velocity and density values based on the literature,[3] a 2D slice at $Y = 310$ was extracted and used as the cranial model for this simulation (Fig. 2(b)). The resulting 2D model has a size of 480×350. Velocity values in the model range from 1440.2 m/s to 2813.7 m/s, with a background velocity of 1500 m/s (water). Density values range from 911 kg/m^3 to 1908 kg/m^3, with a background density of 1000 kg/m^3 (water) (PPW = 3.944, CFL = 0.45).

Cranium–block model This model was designed to evaluate intracranial imaging accuracy (Fig. 2(c)). It was constructed by combining the cranium from the cranial model with the blocks from the block model. The skull component introduces high acoustic impedance interfaces to simulate transcranial propagation, while the block targets are used to assess imaging accuracy and localization precision. The square block is located at (130, 180) and the circular block at (240, 300). Their velocity and density values are identical to those used in the previous two models (PPW = 4.108, CFL = 0.45).

2.5. Stride

All experiments in this paper were conducted using Stride, an open-source Python library designed for solving large-scale ultrasound tomography problems. The FWI framework in Stride was extended to support AWI and SAWI for this paper. Stride offers several advantages for researchers. (i) It is implemented with high-level abstractions and provides comprehensive 2D and 3D medical FWI examples, allowing researchers to initiate experiments efficiently without delving into algorithmic details. (ii) It includes numerous features specifically designed for medical FWI, such as ring-shaped and focused transducers, supporting a wide range of research scenarios. (iii) Its strong parallelization capabilities enable fast execution of FWI simulations, significantly enhancing computational efficiency. (iv) Moreover, it offers flexible and modular interfaces, facilitating convenient program customization and extension.

Stride employs the finite-difference time-domain (FDTD) method, achieving fourth-order accuracy in space and tenth-order accuracy in time. Details about the accuracy of stride can be found in this technical paper.[30] In this paper, all simulations solve the 2D isotropic acoustic wave equation using Stride's numerical solver, with both velocity and density included in the forward modeling. In the inversion, only the velocity is updated to achieve the imaging objective.

All experiments use the same transducer configuration, including transducer geometry, acoustic source settings, number of time steps, time step size, spatial grid spacing, padding region and absorbing boundary conditions.

The transducers used in the experiments are point sources, arranged in an elliptical transducer array provided by Stride. The transducer array is placed along the boundary of the 2D simulation grid, ensuring that the imaging targets are enclosed within the array (Fig. 2). Each experiment uses 128 transducers. In each shot, one transducer serves as the source, and all transducers are used as receivers. In each iteration, gradients are computed using data from eight transducers, each acting once as the source in a full-receive configuration. A complete cycle through all 128 transducers is completed every 16 iterations.

The acoustic source uses Stride's default three-cycle tone burst centered at 500 kHz, which has the same waveform type as that used by Guasch *et al.*,[3] but with a slightly higher central frequency. This higher frequency serves as a better test of the algorithm's stability. A signal sampling interval of 0.08 μs was used, with 2499 samples per shot. The simulation domain includes a perfectly matched layer (PML), with extra and absorbing areas set to (50, 50) and (40, 40), respectively. While these settings are used throughout this study, they are not mandatory. Spatial and temporal discretization parameters can be adapted across imaging modules to meet the dispersion and stability requirements of different modalities.

2.6. Experimental setup

To evaluate SAWI in various contexts, five simulation experiments were designed.

Robustness of SAWI to Gaussian penalty matrix parameters To evaluate the robustness of SAWI to variations in the Gaussian penalty parameter σ, we design a comparative experiment based on the block model. First, AWI is applied to the 100 kHz low-pass filtered data using two different σ values, set to 5% and 20% of the maximum time lag, with 32 iterations performed for each case. To examine whether the imaging error associated with a larger σ value is merely a result of insufficient iterations, an additional 64 iterations are performed, starting from the velocity model obtained with $\sigma = 20\%$. SAWI is then applied to the same low-pass filtered data with σ set to 20% of the maximum time lag, performing 32 iterations in both the pre-node and post-node stages. The results of AWI and SAWI are evaluated through visual inspection of the reconstructed images and analysis of the corresponding Wiener filter curves. Successful imaging is determined based on visual identification of the target in the reconstructed image and Wiener filter curves that exhibit a sharp

peak at zero-time lag with the correct polarity. To facilitate comparison of Wiener filter behavior, each curve is plotted by sampling every fourth trace from the Wiener filters generated by a single source.

Robustness of SAWI in transcranial imaging scenario To evaluate SAWI's performance in transcranial imaging scenarios, a comparative experiment is conducted using the cranial model. We begin by applying conventional AWI to 50 kHz low-pass filtered data with σ set to 5% of the maximum time lag, performing 128 iterations. SAWI is then applied to the same data set and σ setting, with 128 iterations executed in both the pre-node and post-node phases. To verify the effectiveness of the SAWI-generated model, an additional AWI run is performed using 100 kHz low-pass filtered data for 256 iterations, initialized from the velocity model obtained by SAWI with 50 kHz input. The reconstruction results are assessed through visual inspection and analysis of Wiener filter curves. Successful imaging serves as the criterion for evaluating algorithm robustness in transcranial conditions.

Evaluation of SAWI imaging accuracy Next, to evaluate the accuracy of SAWI in transcranial imaging, we apply the method to the cranium–block model. The predicted and observed data are low-pass filtered at 50 kHz, with σ set to 5% of the maximum time lag, and 128 iterations are performed in both the pre-node and post-node phases. To further enable quantitative evaluation, an additional AWI experiment is conducted using 100 kHz low-pass filtered data, initialized from the velocity model reconstructed by SAWI with 50 kHz data and run for 256 iterations. In addition to visual inspection, quantitative analysis is introduced for this experiment. Residual maps between the reconstructed velocity and the ground truth are generated, and the mean squared error (MSE) is computed. Furthermore, velocity profiles are extracted along $X = 130$ (for the square block) and $Y = 300$ (for the circular block). Each profile is plotted with velocity on the y-axis and spatial position on the x-axis, where the spatial coordinate increases from left to right in both directions (i.e., from low to high X or Y).

To evaluate the imaging accuracy of SAWI in transcranial applications, we introduce two metrics: boundary resolution and localization error, both defined based on the reconstructed boundary transitions observed in the velocity profiles. The calculation procedure is described below using the circular block as an example.

(i) In the ground-truth profile, the circular block appears as a square wave. The point where the velocity rises from the background value to the block value is defined as the left boundary (l), and the point where it falls back to the background value is defined as the right boundary (r).

(ii) Due to the limited resolution of inversion, the reconstructed boundary transitions appear as sloped segments instead of ideal step edges. For each boundary, we identify the ramp top (t) as the maximum velocity point and the ramp base (b) as the minimum velocity point along the monotonic slope that intersects the corresponding ground-truth boundary. Four positions for each block are obtained: x_{lt}, x_{lb}, x_{rt}, x_{rb} (Fig. 3).

(iii) Boundary resolution is defined as

$$\mathrm{Resolution}_{\mathrm{Boundary}} = \max\left(\left|x_{\mathrm{lt}} - x_{\mathrm{lb}}\right|, \left|x_{\mathrm{rt}} - x_{\mathrm{rb}}\right|\right) \times \Delta x. \quad (15)$$

(iv) The localization error is composed of left boundary position error, right boundary position error and distance error, which are defined as

$$x_{\mathrm{l}} = \frac{(x_{\mathrm{lt}} + x_{\mathrm{lb}})}{2}, \quad x_{\mathrm{r}} = \frac{(x_{\mathrm{rt}} + x_{\mathrm{rb}})}{2}, \quad (16)$$

$$\mathrm{Error}_{\mathrm{Left\ boundary\ position}} = \frac{x_{\mathrm{l}} - x_{\mathrm{l_groundtruth}}}{x_{\mathrm{l_groundtruth}}}, \quad (17)$$

$$\mathrm{Error}_{\mathrm{right\ boundary\ position}} = \frac{x_{\mathrm{r}} - x_{\mathrm{r_groundtruth}}}{x_{\mathrm{r_groundtruth}}}, \quad (18)$$

$$\mathrm{Error}_{\mathrm{distance}} = \frac{|x_{\mathrm{l}} - x_{\mathrm{r}}|}{\left|x_{\mathrm{l_groundtruth}} - x_{\mathrm{r_groundtruth}}\right|}. \quad (19)$$

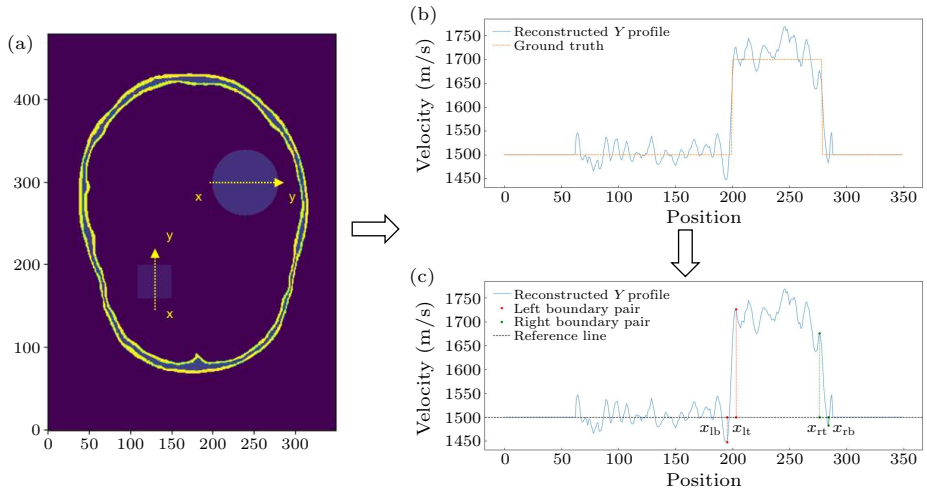


Fig. 3. Calculation process of x_{lt}, x_{lb}, x_{rt}, and x_{rb}.

Comparison between SAWI and AWI To investigate the difference in reconstruction accuracy between SAWI and AWI, as well as the potential increase in computational cost introduced by SAWI due to its lower imaging accuracy in the pre-checkpoint stage, we design a comparative experiment. SAWI and AWI are both applied to the block model, using data that are low-pass filtered at 100 kHz for inversion. For SAWI, the pre-node stage includes 32 iterations with pseudo-Hessian preconditioning, using σ set to 20% of the maximum time lag. The post-node stage consists of another 32 iterations without preconditioning, where σ is set to 5% of the maximum time lag. For AWI, the inversion process consists of 32 iterations with preconditioning followed by 32 iterations without preconditioning, with σ consistently set to 5% of the maximum time lag. Reconstruction accuracy is evaluated using MSE, while the computational cost is assessed by analyzing the MSE curve with respect to the number of iterations.

Comparison between SAWI and FWI Finally, to investigate the differences between SAWI and conventional FWI in imaging performance, both methods are applied to the block model under identical settings. Both algorithms employ a multi-scale inversion scheme, performing 32 iterations on low-pass filtered data (100 kHz) and another 32 iterations on band-pass filtered data (100–200 kHz). For SAWI's inversion of the 100 kHz data, the pre-node stage includes 16 iterations with pseudo-Hessian preconditioning, using σ set to 20% of the maximum time lag. Then, it is followed by the post-node stage of 16 iterations without preconditioning, with σ set to 5% of the maximum time lag. Subsequently, 32 iterations without preconditioning are conducted on the 100–200 kHz band-pass filtered data, with σ set to 5% of the maximum time lag. The same preconditioning operation is applied during the FWI iteration process. To facilitate a more comprehensive comparison, the final imaging results of both SAWI and FWI are visualized, along with residual maps between the reconstructions and the ground truth at the end of each frequency band. In addition, velocity distribution profiles along $X = 110$ and $Y = 250$ are extracted from both SAWI and FWI results for direct comparison.

3. Results

3.1. Robustness of SAWI to Gaussian penalty matrix parameters

We first use conventional AWI to image the block model under two Gaussian penalty σ parameters: 5% and 20% of the maximum time lag. The result shows that AWI successfully reconstructs the image with σ corresponding to 5% (Fig. 4(a)). In contrast, when using σ corresponding to 20%, the circular target's contour size and internal velocity values (Fig. 4(b)) deviate significantly from the ground truth (Fig. 4(d)).

To investigate whether the poor results with the 20% parameter are due to insufficient iterations, we extend the AWI to 64 iterations under the same parameters. The results (Fig. 4(c)) reveal that increasing the number of iterations does not improve image quality. The anomalies in the circular target remain unresolved, suggesting that AWI likely converges to a local minimum.

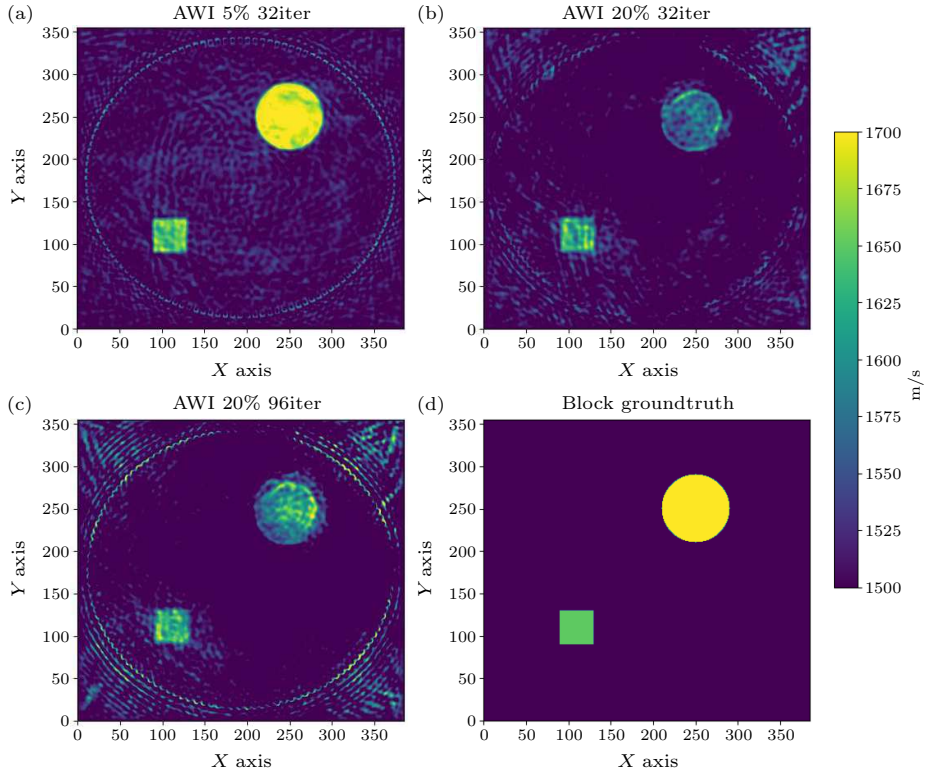


Fig. 4. Imaging results of the block model by AWI with different σ settings and inversion iterations: (a) 5% with 32 iterations, (b) 20% with 32 iterations, (c) 20% with 96 iterations. (d) Ground truth.

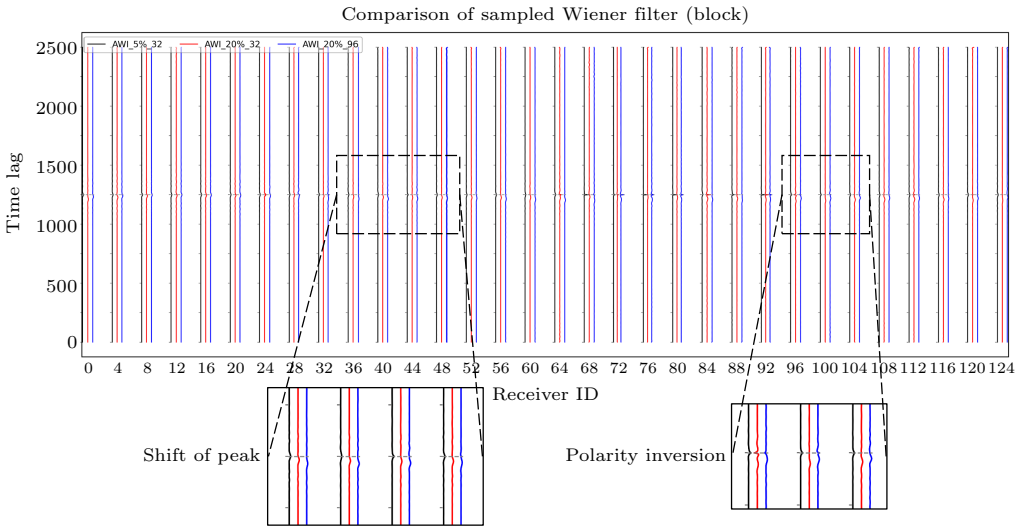


Fig. 5. Wiener filter plot corresponding to the results in Fig. 4.

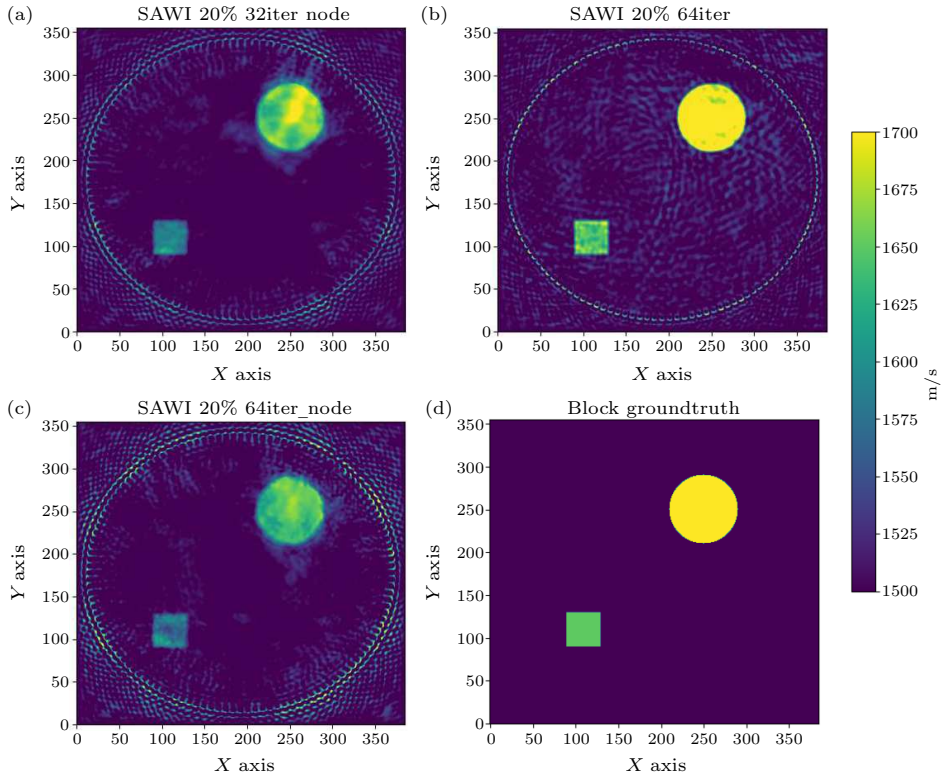


Fig. 6. SAWI imaging results for the block model under σ corresponding to 20%. (a) 32 iterations before the node. (b) Result (a) followed 32 iterations after the node. (c) 64 iterations before the node. (d) Ground truth.

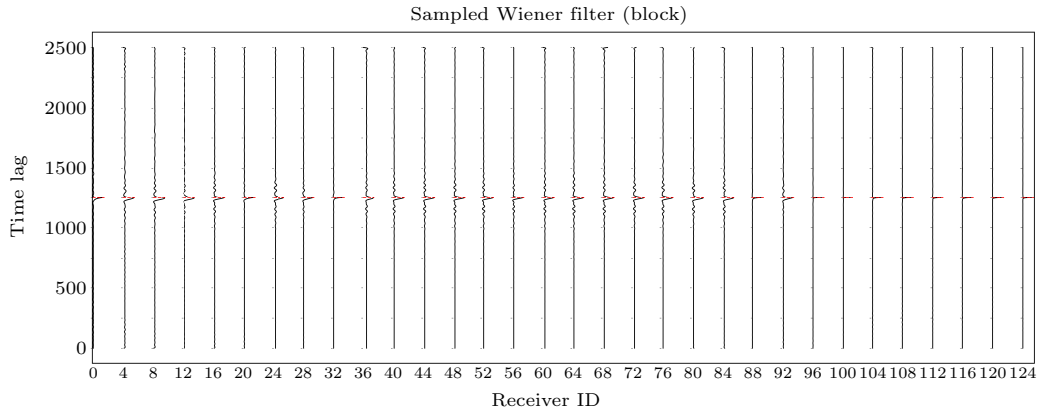


Fig. 7. Wiener filter plot corresponding to the final imaging results of SAWI.

The corresponding Wiener filters for Figs. 4(a)–4(c) are shown in Fig. 5. For σ corresponding to 20%, even after 64 additional iterations, the Wiener filter still exhibits peak dispersion and polarity reversal, indicating that further iterations will not enable AWI to achieve accurate imaging.

We then apply SAWI to the block model with σ set to 20% of the maximum time lag. The imaging results at the node and after complete inversion are shown in Fig. 6. At the node (Fig. 6(a)), while the velocity values and the circular shape exhibit deviations from the ground truth, no spurious circular artifacts are observed such as those seen in conventional AWI. These deviations are limited and primarily manifest as mild smoothing around the target boundaries. In the final imaging result (Fig. 6(b)), both the square and circular blocks are accurately recovered with well-defined boundaries, correct positions, and velocity values closely matching the ground truth. This result is consistent with that of conventional AWI under a smaller σ value (5%), indicating that SAWI maintains robustness even under less favorable parameter settings. The corresponding sampled Wiener filter plot is shown in Fig. 7, where the position indicated by the red dashed line corresponds to the zero-lag location. The Wiener filter plot further confirms that SAWI achieves successful imaging. To investigate the imaging performance of the method used before the node, 64 iterations are performed using this method. The result (Fig. 6(c)) shows that while this approach is more robust than conventional AWI, it fails to produce accurate imaging results. This method is therefore only suitable for providing an initial model for SAWI.

3.2. Robustness of SAWI in transcranial imaging scenario

We first use conventional AWI to image the cranial model under σ set to 5% of the maximum time lag. After 128 iterations, the result (Fig. 8(a)) shows a complete failure in imaging. This is also evident from the Wiener filter (Fig. 9), which displays significant polarity reversal and negative peaks that hinder imaging.

Next, we apply SAWI to the cranial model. The imaging results at the node and after the full inversion are shown in Figs. 8(b) and 8(c). At the node, the result already produces a high-quality initial model with clearly defined and accurately located cranial contours. Basic outlines of internal structures are also faintly discernible. The full inversion result shows significant improvement in clarity compared to the node result, with enhanced contrast in soft tissue regions. The Wiener filter results further support the effectiveness of SAWI (Fig. 9). Although some traces exhibit smaller peaks, no polarity reversal or negative peaks that hinder imaging are observed, unlike in conventional AWI. To further assess the performance, we increase the frequency to 100 kHz and perform an additional 256 iterations, see Figs. 8(d) and 8(e). The results show a substantial improvement in clarity and accuracy, confirming that SAWI produces reliable results for transcranial imaging.

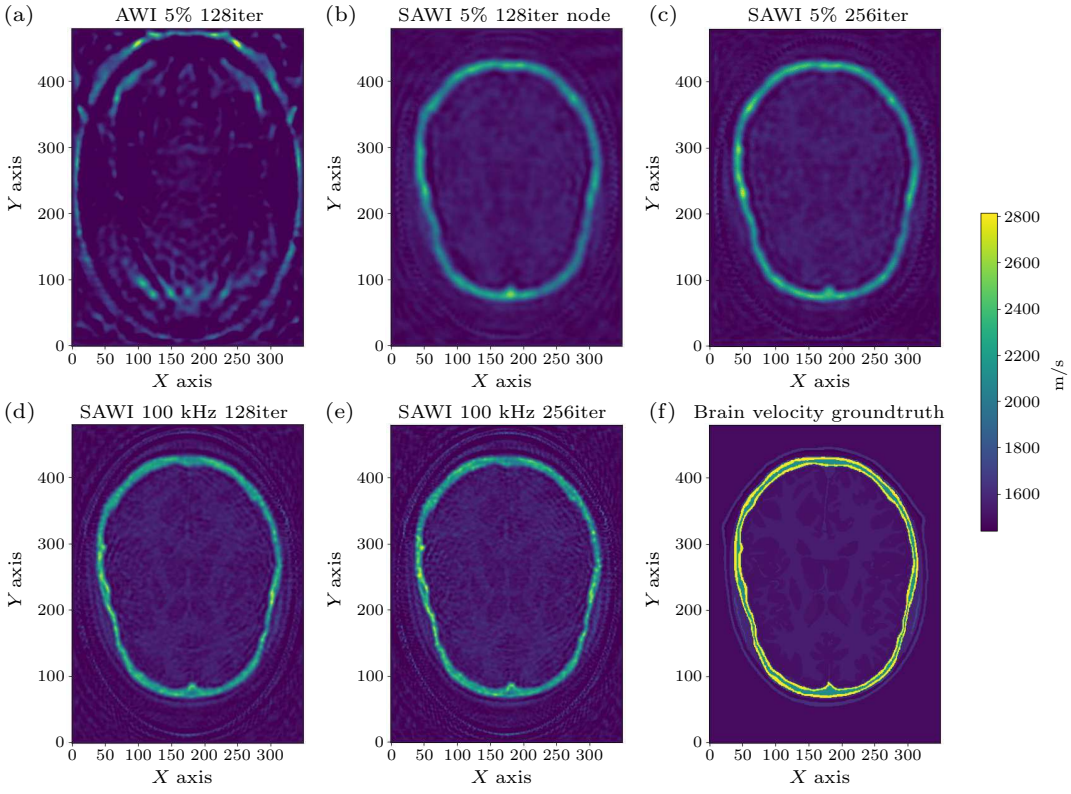


Fig. 8. Comparison of AWI and SAWI imaging results for cranial brain models. (a) AWI with 128 iterations. (b) SAWI before node 128 iterations. (c) Result (b) followed 128 iterations after the node. (d) Result (c) followed AWI with 128 iterations. (e) Result (c) followed AWI with 256 iterations. (f) Ground truth.

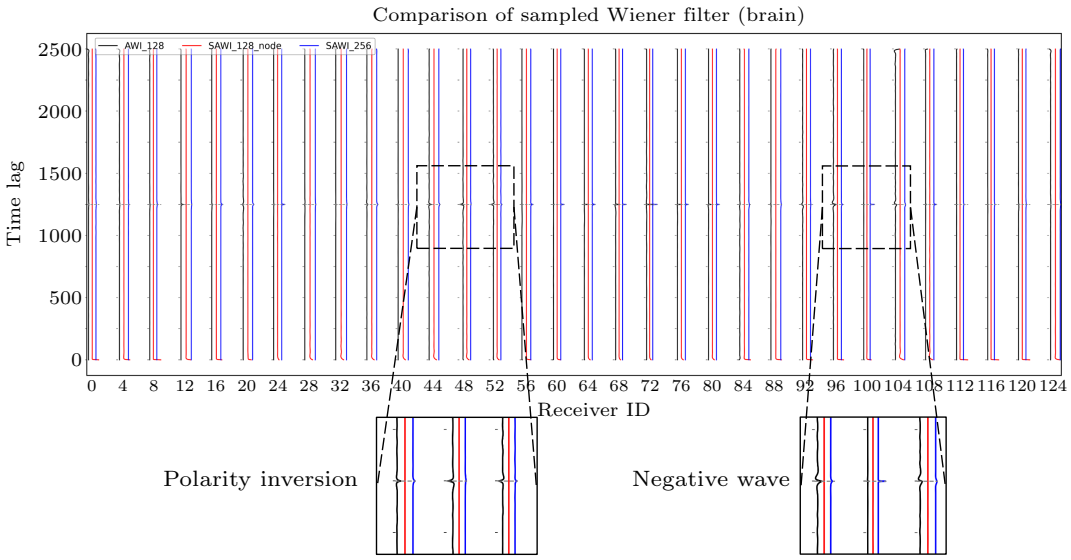


Fig. 9. Wiener filter plot corresponding to the results in Figs. 8(a)–8(c).

3.3. Evaluation of SAWI imaging accuracy

SAWI is applied to the cranium–block model using data filtered at 50 kHz, with results at the node and after full inversion shown in Figs. 10(a) and 10(b). The reconstruction successfully recovers both the skull and the blocks, with shapes and positions consistent with the ground truth. When the low-pass filter cutoff is increased to 100 kHz (Fig. 10(c)), the reconstruction demonstrates a notable improvement in both boundary sharpness and target localization. To quantitatively assess the imaging accuracy, the error maps and corresponding profiles are shown in Fig. 11, and the boundary resolution and boundary localization metrics for both the 50 kHz and 100 kHz full inversion results are summarized in Table 1. It could be seen that SAWI achieves satisfactory imaging accuracy even at 50 kHz, with boundary resolution reaching the millimeter level. When the frequency is increased to 100 kHz, both resolution and localization accuracy improve further, as expected. These results confirm that the enhanced robustness of SAWI does not come at the cost of reduced imaging precision, and that the method can effectively benefit from higher-frequency content.

3.4. Comparison between SAWI and AWI

The imaging results are shown in Fig. 12. Visually, it is difficult to distinguish significant differences between SAWI and AWI, although AWI appears to exhibit slightly more pronounced artifacts compared to SAWI. The residual maps between the reconstructed results and the ground truth after 32 and 64 iterations for both SAWI and AWI are also presented (Fig. 13). It can be observed that although the MSE of SAWI at the checkpoint is considerably higher than that of AWI, the final reconstruction MSE of SAWI is slightly better.

The MSE versus iteration curves for the final 32 iterations (iterations 33–64) without preconditioning are plotted for both

Table 1. Boundary resolution and accuracy of Figs. 10(b) and 10(c).

Accuracy index	SAWI_50k_256	SAWI_100k_256
Square		
Boundary resolution (mm)	12	6
$\text{Error}_{\text{Left boundary position}}$	0.62%	0.62%
$\text{Error}_{\text{Right boundary position}}$	0.25%	0.50%
$\text{Error}_{\text{Distance}}$	1.25%	0.00%
Circle		
Boundary resolution (mm)	11	8
$\text{Error}_{\text{Left boundary position}}$	1.25%	0.50%
$\text{Error}_{\text{Right boundary position}}$	0.00%	0.00%
$\text{Error}_{\text{Distance}}$	3.12%	1.25%

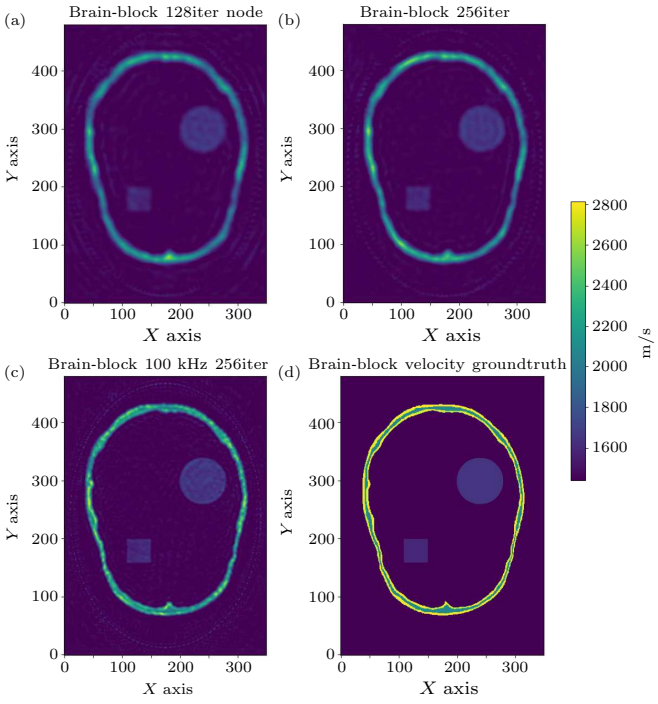


Fig. 10. Plot of SAWI imaging results for the cranium–block model. (a) 50 kHz before node 128 iterations. (b) Result B followed 128 iterations after node. (c) Result (b) followed AWI with 256 iterations. (d) Ground truth.

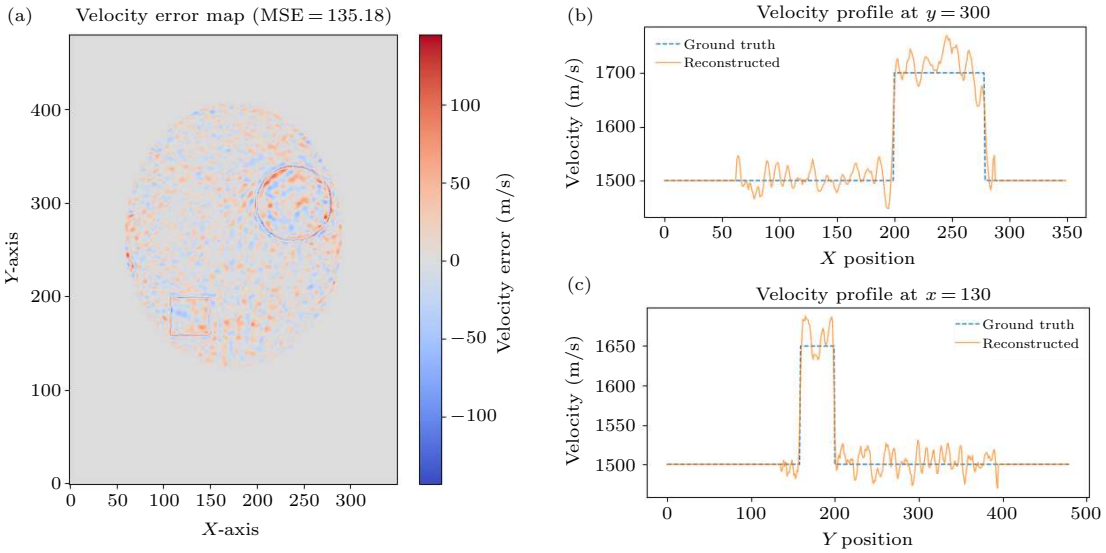


Fig. 11. Quantitative analysis plot of Fig. 10(c).

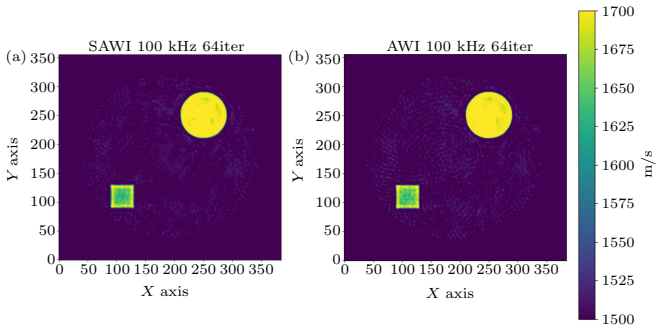


Fig. 12. SAWI and AWI imaging results for the block model.

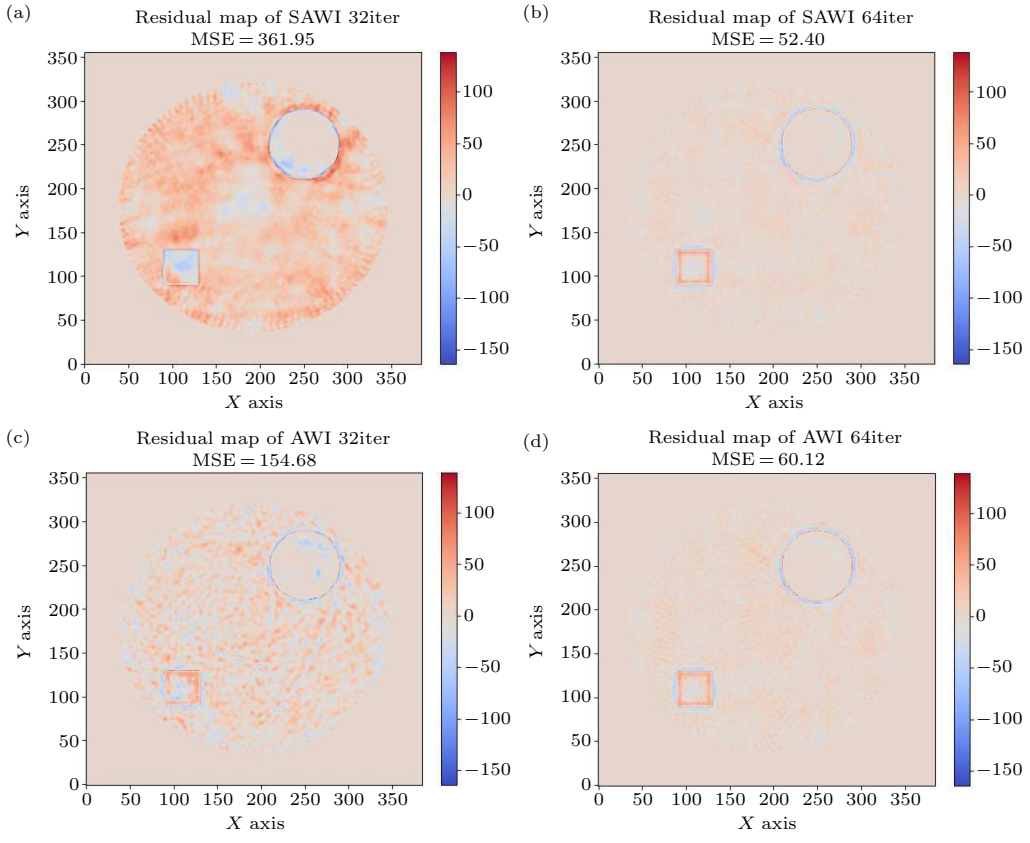


Fig. 13. Residual maps of SAWI and AWI imaging results at the 32th and 64th iterations.

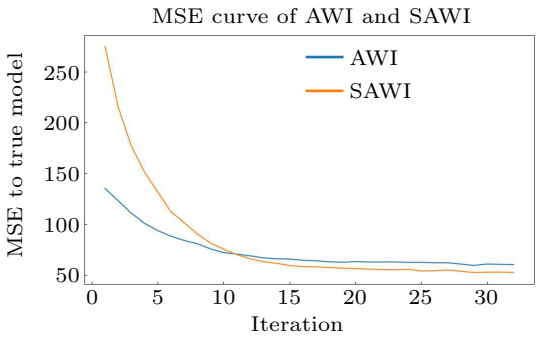


Fig. 14. MSE curves of SAWI and AWI reconstruction results versus iteration number.

SAWI and AWI, as shown in Fig. 14. The results show that SAWI experiences a delay of approximately 11 iterations in this experiment. This delay is related to the total number of iterations and the allocation of iterations before and after the checkpoint in SAWI, and can potentially be optimized.

Moreover, since SAWI adopts exactly the same configuration as AWI in the post-node stage, SAWI appears to exhibit a stable MSE advantage compared with conventional AWI.

3.5. Comparison between SAWI and FWI

The final reconstruction results of SAWI and FWI are shown in Fig. 15. It can be observed that although SAWI still exhibits noise-like artifacts, the boundaries of both the circular and square inclusions are reconstructed more sharply. The residual maps corresponding to the 32nd iteration (0–100 kHz band) and the 64th iteration (100–200 kHz band) are also presented (Fig. 16). To better evaluate the imaging performance, a masking operation was applied to focus solely on the two inclusion regions when calculating MSE and analyzing the results. The results indicate that SAWI demonstrates a clear advantage over FWI at the initial frequency band. However, as the frequency increases and iterations continue, FWI gradually overtakes SAWI. From the velocity profiles (Fig. 17), it can be seen that FWI provides smoother and more stable curves overall, but its slope at the square boundary is lower than that of SAWI, indicating a slightly lower boundary resolution compared to SAWI.

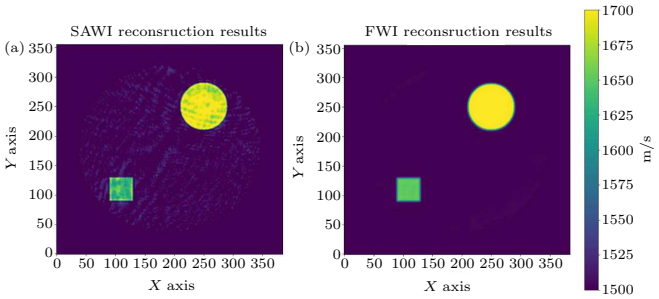


Fig. 15. SAWI and FWI imaging results for the block model.

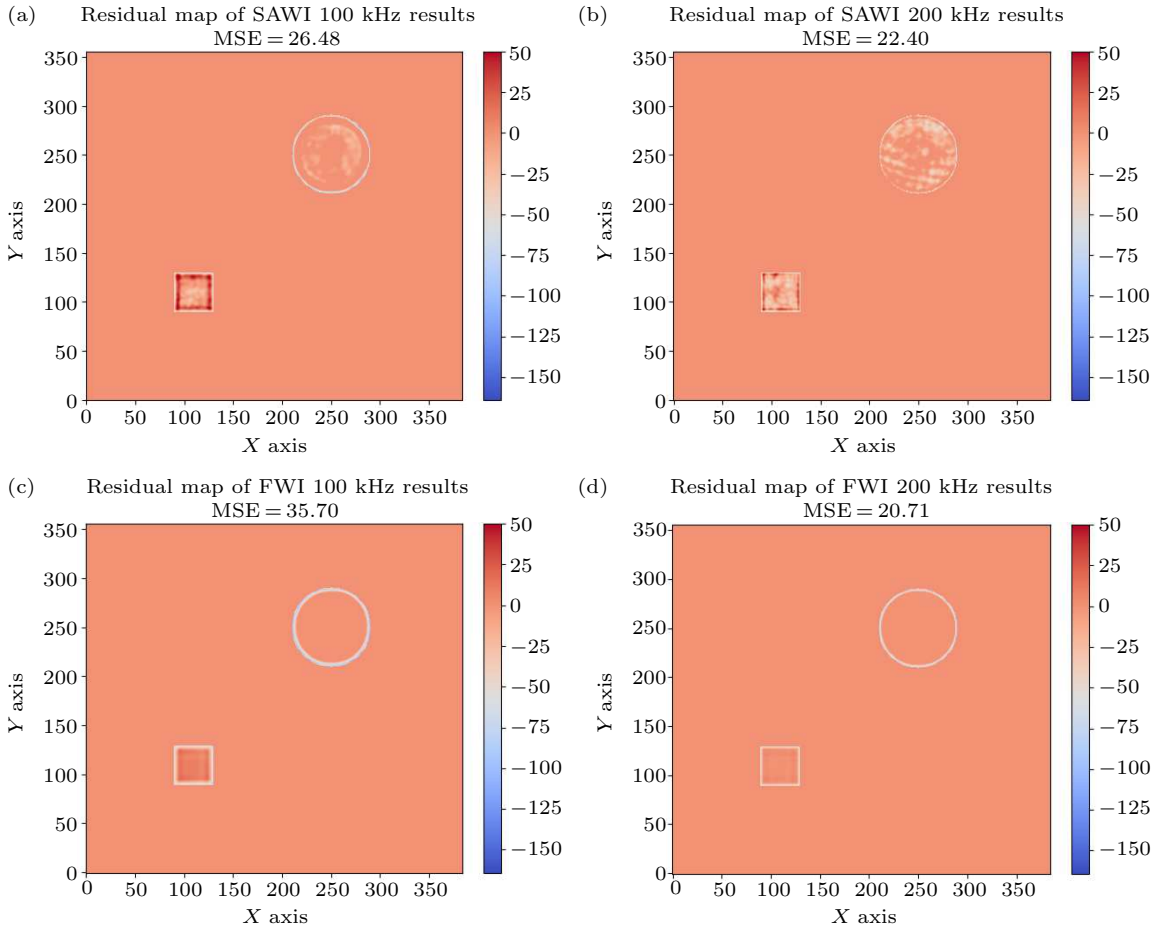


Fig. 16. Residual maps of SAWI and FWI imaging results at the 32th and 64th iterations.

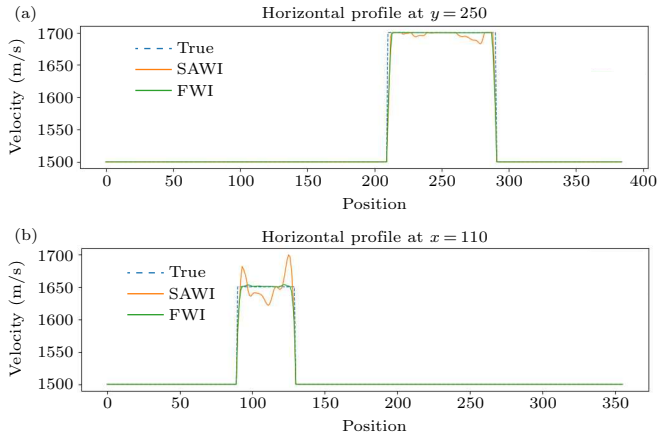


Fig. 17. Velocity profiles of reconstruction results using SAWI and FWI.

4. Conclusion and perspectives

Achieving high-resolution brain imaging in a portable and safe manner is essential for monitoring neurological conditions. The FWI variant, AWI, has shown potential for inverting 3D brain acquisition data. However, the selection of parameters in the Gaussian penalty function, particularly the width (σ), strongly influences AWI's imaging performance, and conventional AWI struggles to achieve reliable imaging in transcranial scenarios. To address these challenges, we propose a method that modifies the construction of the Wiener filter's zero-lag position. This approach significantly enhances the robustness of AWI in these scenarios without altering its framework or increasing computational costs.

Discussion of experimental results This paper constructed three models to evaluate the proposed method from different perspectives: its robustness to parameter selection, applicability to transcranial scenarios and accuracy in transcranial imaging. First, the block model is used to show the effect of the Gaussian penalty matrix σ value on AWI imaging. This problem is consistent with the findings of Pladys *et al.*[25] Conventional AWI typically employs either linear or Gaussian penalty matrices. In the simulations, we find that constructing a maximization optimization problem and using a Gaussian penalty matrix both have advantages over the alternative in terms of the iteration speed of the velocity values. This might explain why these combinations are frequently used in AWI research for describing conventional AWI and conducting comparative experiments.[14,24,25,27,31]

The strong dependence of successful imaging on parameter tuning suggests that the algorithm lacks robustness under certain configurations. In the medical field, where both accuracy and robustness are critical, this instability can hinder the broader application of AWI. In addition, the computational cost of AWI remains non-negligible compared to FWI,[3] and the linear penalty matrix can further slow the imaging process of AWI, affecting its practical use. Therefore, the method proposed in this paper is necessary for improving AWI's robustness to parameter tuning. The experimental results show that SAWI significantly enhances the robustness of AWI to Gaussian penalty matrix parameter choices. Further experiments indicate that SAWI can still produce images for the block model even when σ is set to 50% of the maximum time lag, demonstrating the method's contribution to improving the robustness of AWI.

Then, the cranial model is used to illustrate the difficulties AWI encounters in transcranial imaging. In practice, we find that with the configurations used, AWI fails to produce an image for the transcranial scenario when σ is set to 5% of the maximum lag. Even reducing σ to 2% of the maximum lag does not enable successful imaging. We also replace the Gaussian penalty matrix with a linear penalty matrix. However, even after 256 iterations with 50 kHz filtered data followed by another 256 iterations with 100 kHz filtered data, the shape of the skull is still far from the ground truth. We also explore the impact of source wavelet frequency on imaging results. Even when the source wavelet frequency is reduced to 200 kHz, no indication of successful transcranial imaging using conventional AWI is observed under the previous experimental settings. This suggests that AWI's failure in this scenario is not solely due to the choice of σ. The proposed method effectively addresses this issue. Without increasing computational costs, SAWI achieves transcranial imaging simply by modifying the zero-lag position of the Wiener filter. Furthermore, the imaging accuracy can be improved by integrating MDWI,[19] which reduces the length of the Wiener filter to achieve faster and more accurate imaging. This highlights the advantages of SAWI over conventional AWI in transcranial scenarios.

In addition, the cranium–block model is used to demonstrate the imaging accuracy of SAWI in transcranial imaging scenarios. The results show high accuracy in both resolution and localization, suggesting that SAWI's robustness to parameter selection and transcranial conditions does not seem to negatively impact its imaging accuracy.

SAWI was compared with conventional AWI under identical experimental settings. The results show that although SAWI exhibits some imaging lag relative to AWI due to the pre-node imaging approach, it achieves a lower MSE than AWI at the same number of iterations. Using the pre-node imaging result as the initial model appears to enable faster convergence of AWI.

Finally, the imaging performance of SAWI is compared to that of conventional FWI under identical experimental conditions. The results show that SAWI has an absolute advantage in MSE over FWI at the initial frequency band. However, the higher stability of FWI allows it to benefit more from the multiscale inversion strategy. In addition, SAWI demonstrates a resolution advantage compared to FWI. These findings are consistent with previous observations.[27] Since the second inversion phase of SAWI is identical to conventional

AWI, its accuracy benefits from the same resolution potential while overcoming the limitations in stability and convergence. Further accuracy improvements can be achieved by coupling SAWI with FWI[3] or MDWI.[19]

Potential reasons for increased stability The instability of AWI compared to FWI primarily stems from two factors. First, the AWI objective function does not consider the polarity of $\boldsymbol{w}$, allowing negative components to appear in $\boldsymbol{w}$. Second, AWI aims to transform the Wiener filter into a unit impulse function at the zero-lag position. Ideally, the discrete form of $\boldsymbol{w}$ should have a value of 1 at the zero-lag position and 0 elsewhere, which is not inherently difficult to achieve. However, since $\boldsymbol{P}^{\mathrm{T}}\boldsymbol{P}$ may be ill-conditioned or singular, a small positive value is added to its diagonal to ensure numerical stability when solving for $\boldsymbol{w}$. This adjustment causes the ideal form of $\boldsymbol{w}$ to deviate from a unit impulse function, becoming a small wavelet centered at the zero-lag position.

This instability is even more pronounced compared to the objective of FWI, which aims to minimize the residual between predicted and observed data to zero. In AWI, the optimization process squeezes the energy of $\boldsymbol{w}$ towards the zero-lag position. If negative components emerge during this process, the $\boldsymbol{w}$ may become a negatively polarized wavelet. This outcome opposes the polarity of the ideal form of $\boldsymbol{w}$ yet aligns with its optimization logic, leading to inaccurate imaging.

To address this limitation of AWI, previous research, such as the work by Yao,[24] has introduced constraints to ensure that $\boldsymbol{w}$ remains positive. By adding a positivity constraint to $\boldsymbol{w}$ and solving it through an iterative least-squares method, this approach significantly enhances the stability and accuracy of AWI. However, this method incurs prohibitively high computational costs since $\boldsymbol{w}$ must be solved iteratively for every computation, greatly reducing its practical value. In the SAWI method proposed in this paper, we address this issue by shifting the zero-lag position of the Wiener filter to the edge. This adjustment transforms the ideal form of $\boldsymbol{w}$ from a symmetric wavelet centered at zero lag into a unilateral curve with energy concentrated near the edge. Instead of shaping $\boldsymbol{w}$ into a symmetric peak, the objective becomes simply pushing energy towards one side. This simplification may explain the observed increase in AWI's robustness.

Moreover, constructing the Wiener filter as a unilateral form does not imply losing information from the opposite time direction. The lag information from the other side still influences the waveform, although the correspondence between the lag number and the peak position in $\boldsymbol{w}$ becomes less explicit. This limitation is reflected in the reduced accuracy of pre-node imaging.

Limitations The method proposed in this paper significantly improves AWI's stability in Gaussian penalty matrix parameter selection and transcranial imaging scenarios. However, it has several limitations. The core limitation lies in the fact that this method does not completely eliminate the issue of negative polarity in AWI. Instead, it enhances AWI's robustness to Gaussian penalty matrix parameter choices and transcranial scenarios by simplifying the target form of the Wiener filter. A more sophisticated approach is still required to fundamentally resolve AWI's deficiencies.

Although the method is implemented using the highly parallelized Stride Python library and does not increase the per-iteration computational cost compared to conventional AWI, another limitation is the inherent computational burden of AWI, which has been widely discussed in previous studies and will not be elaborated upon here.[3,19] Since the purpose of this paper is to investigate the imaging capabilities of the proposed method, noise and viscoelastic effects were not introduced. Finally, this study did not perform density inversion, which could be beneficial for further exploration of transcranial imaging performance.[32]

Acknowledgments

Project supported by the National Natural Science Foundation of China (Grant No. 82151302), the National High Level Hospital Clinical Research Funding (Grant No. 2022-PUMCH-B-113), the National High Level Hospital Clinical Research Funding (Grant No. 2022-PUMCH-A-019), and the CAMS Innovation Fund for Medical Sciences (Grant No. 2021-12M-1-014).

References

[1] Ivanov M, Wilkins S, Poeata I and Brodbelt A 2010 *Br. J. Neurosurg.* **24** 510
[2] Smith S W, Ivancevich N M, Lindsey B D, Whitman J, Light E, Fronheiser M, Nicoletto H A and Laskowitz D T 2009 *Ultrasound Med. Biol.* **35** 329
[3] Guasch L, Calderón Agudo O, Tang M X, Nachev P and Warner M 2020 *NPJ Digit. Med.* **3** 28
[4] Edlow B L, Mareyam A, Horn A, Polimeni J R, Witzel T, Tisdall M D, Augustinack J C, Stockmann J P, Diamond B R, Stevens A, Tirrell L S, Folkerth R D, Wald L L, Fischl B and van der Kouwe A 2019 *Sci. Data* **6** 244
[5] Yanagawa M, Hata A, Honda O, Kikuchi N, Miyata T, Uranishi A, Tsukagoshi S and Tomiyama N 2018 *Eur. Radiol.* **28** 5060
[6] Menikou G, Dadakova T, Pavlina M, Bock M and Damianou C 2015 *Ultrasonics* **57** 144
[7] Chen T, Liu L, Ma X, Zhang Y, Liu H, Zheng R, Ren J, Zhou H, Ren Y, Gao R, Chen N, Zheng H, Song L and Liu C 2022 *IEEE Trans. Biomed. Eng.* **69** 1093
[8] Emberson J, Lees K R, Lyden P, Blackwell L, Albers G, Bluhmki E, Brott T, Cohen G, Davis S, Donnan G, Grotta J, Howard G, Kaste M, Koga M, von Kummer R, Lansberg M, Lindley R I, Murray G, Olivot J M, Parsons M, Tilley B, Toni D, Toyoda K, Wahlgren N, Wardlaw J, Whiteley W, del Zoppo G J and Baigent C 2014 *Lancet* **384** 1929
[9] Lauzier P T and Chen G H 2013 *Med. Phys.* **40** 021902
[10] Comeau R M, Sadikot A F, Fenster A and Peters T M 2000 *Med. Phys.* **27** 787
[11] Letteboer M M, Willems P W, Viergever M A and Niessen W J 2005 *IEEE Trans. Biomed. Eng.* **52** 268
[12] Maurer C R Jr, Hill D L, Martin A J, Liu H, McCue M, Rueckert D, Lloret D, Hall W A, Maxwell R E, Hawkes D J and Truwit C L 1998 *IEEE Trans. Med. Imaging* **17** 817
[13] Nimsky C, Ganslandt O, Cerny S, Hastreiter P, Greiner G and Fahlbusch R 2000 *Neurosurgery* **47** 1070
[14] Guasch L, Warner M and Ravaut C 2019 *Geophysics* **84** R447

[15] Ren J, Li J, Chen S, Liu Y and Ta D 2025 *Ultrasonics* **145** 107465

[16] Wiskin J W, Borup D T, Iuanow E, Klock J and Lenox M W 2017 *IEEE Trans. Ultrason. Ferroelectr. Freq. Control* **64** 1161

[17] Sandhu G Y, Li C, Roy O, Schmidt S and Duric N 2015 *Phys. Med. Biol.* **60** 5381

[18] Wiskin J, Malik B, Borup D, Pirshafiey N and Klock J 2020 *Sci. Rep.* **10** 20166

[19] Li Y B, Wang J, Su C, Lin W J, Wang X M and Luo Y 2023 *Chin. Phys. B* **32** 014303

[20] Bunks C, Saleck F M, Zaleski S and Chavent G 1995 *Geophysics* **60** 1457

[21] Jiang C, Li B, Xie L, Liu C, Xu K, Zhan Y and Ta D 2023 *Ultrasonics* **135** 107124

[22] Ren J, Wang X, Liu C, Sun H, Tong J, Lin M, Li J, Liang L, Yin F, Xie M and Liu Y 2023 *Sensors* **23** 8341

[23] Robins T, Camacho J, Agudo O C, Herraiz J L and Guasch L 2021 *Sensors* **21** 4570

[24] Yao J 2019 *Adaptive Waveform Inversion: Algebraic Interpretation, Convergence Analysis and Alternative Formulations* (PhD Thesis) (London: Imperial College London)

[25] Pladys A, Brossier R, Li Y and Métivier L 2021 *Geophysics* **86** R563

[26] Chen W, Tao C, Hu Z, Yuan S, Liu Q and Liu X 2022 *Chin. Phys. B* **31** 044304

[27] Warner M and Guasch L 2016 *Geophysics* **81** R429

[28] Courant R, Friedrichs K and Lewy H 1967 *IBM J. Res. Dev.* **11** 215

[29] Iacono M I, Neufeld E, Akinnagbe E, Bower K, Wolf J, Vogiatzis Oikonomidis I, Sharma D, Lloyd B, Wilm B J, Wyss M, Pruessmann K P, Jakab A, Makris N, Cohen E D, Kuster N, Kainz W and Angelone L M 2015 *PLoS One* **10** e0124126

[30] Cueto C, Bates O, Strong G, Cudeiro J, Luporini F, Calderón Agudo Ò, Gorman G, Guasch L and Tang M X 2022 *Comput. Methods Programs Biomed.* **240** 107710

[31] Eaid M, Keating S and Innanen K https://www.crewes.org/Documents/ResearchReports/2018/CRR201809.pdf

[32] Li Y, Shi Q, Li Y, Song X, Liu C, Ta D and Wang W 2021 *Chin. Phys. B* **30** 014302